

**Experimental validation of phase space conduits of transition between potential wells**Shane D. Ross,<sup>1</sup> Amir E. BozorgMagham,<sup>1</sup> Shibabrat Naik,<sup>1,\*</sup> and Lawrence N. Virgin<sup>2</sup><sup>1</sup>*Engineering Mechanics Program, Virginia Tech, Blacksburg, Virginia 24061, USA*<sup>2</sup>*Mechanical Engineering and Materials Science, Duke University, Durham, North Carolina 27708, USA*

(Received 17 April 2018; revised manuscript received 30 August 2018; published 15 November 2018)

A phase space boundary between transition and nontransition trajectories, similar to those observed in Hamiltonian systems with rank-1 saddles, is verified experimentally in a macroscopic system. We present a validation of the phase space flux across rank-1 saddles connecting adjacent potential wells, and we confirm the underlying phase space conduits that mediate the transition. Experimental regions of transition are found to agree with the theory to within 1%, suggesting the robustness of phase space conduits of transition in a broad array of two or more degrees of freedom experimental systems, despite the presence of small dissipation.

DOI: [10.1103/PhysRevE.98.052214](https://doi.org/10.1103/PhysRevE.98.052214)**I. INTRODUCTION**

Prediction of transition events and the determination of governing criteria has significance in many physical, chemical, and engineering systems where rank-1 saddles are present. Some examples of such systems include ionization of a hydrogen atom under an electromagnetic field in atomic physics [1], transport of defects in solid-state and semiconductor physics [2], isomerization of clusters [3], reaction rates in chemical physics [4,5], buckling modes in structural mechanics [6,7], ship motion and capsize [8–10], escape and recapture of comets and asteroids in celestial mechanics [11–13], and escape into inflation or recollapse to singularity in cosmology [14]. The theoretical criteria of transition and its agreement with laboratory experiment have been shown for one degree-of-freedom (DOF) systems [15–17]. Detailed experimental validation of the geometrical framework for predicting transition in higher dimensional phase space ( $\geq 4$ , that is, for two or more DOF systems) is still lacking. The geometric framework of phase space conduits in such systems, termed tube dynamics [11,12,18,19], has not been demonstrated in a laboratory experiment. It is noted that similar notions of transition were developed for idealized microscopic systems, particularly chemical reactions [1,20–22] under the terms of transition state and reactive island theory. However, investigations of the predicted phase space conduits of transition between wells in a multiwell system have stayed within the confines of numerical simulations. In this paper, we present a direct experimental validation of the accuracy of the phase space conduits, as well as the transition fraction obtained as a function of energy, in a four dimensional phase space using a controlled laboratory experiment of a macroscopic system.

In [23–25], experimental validation of global characteristics of one DOF Hamiltonian dynamics of scalar transport has been accomplished using direct measurement of the Poincaré

stroboscopic sections using dye visualization of the fluid flow. In [23,24], the experimental and computational results of chaotic mixing were compared by measuring the observed and simulated distribution of particles, thus confirming the theory of chaotic transport in Hamiltonian systems for such systems. Our objective is to validate theoretical predictions of transition between potential wells in an exemplar experimental 2 DOF system, where qualitatively different global dynamics can occur. Our setup consists of a mass rolling on a multiwell surface that is representative of potential energy underlying systems that exhibit transition and escape behavior. The archetypal potential energy surface chosen has implications in transition, escape, and recapture phenomena in many of the aforementioned physical systems. In some of these systems, transition in the conservative case has been understood in terms of trajectories of a given energy crossing a hypersurface or transition state (bounded by a normally hyperbolic invariant manifold of geometry  $S^{2N-3}$  in  $N$  DOF). In this paper, for  $N = 2$ , trajectories pass inside a tubelike separatrix, which has the advantage of accommodating the inclusion of nonconservative forces such as stochasticity and damping [7,10]. The semianalytical geometry-based approach for identifying transition trajectories has also been considered for periodically forced 2 DOF systems in [26,27]. Our analytical approach here focuses on identifying separatrices from the unforced dynamics, and it generalizes to higher-dimensional phase space [5,28]. Based on the illustrative nature of our laboratory experiment of a 2 DOF mechanical system, and the generality of the framework to higher degrees of freedom [19], we envision that the geometric approach demonstrated here can apply to experiments regarding transition across rank-1 saddles in three or more DOF systems in many physical contexts.

**II. SEPARATRICES in  $N$  DOF**

To begin the mathematical description of the invariant manifolds that partition the  $2N$ -dimensional phase space, we perform a linear transformation of the underlying conservative Hamiltonian. This transformation involves a translation of the

\*Author to whom all correspondence should be addressed: shiba@vt.edu

saddle equilibrium point to the origin and a linear change of coordinates that uses the eigenvectors of the linear system. The resulting Hamiltonian near the saddle has the quadratic (normal) form

$$H_2(q_1, p_1, \dots, q_N, p_N) = \lambda q_1 p_1 + \sum_{k=2}^N \frac{\omega_k}{2} (q_k^2 + p_k^2), \quad (1)$$

where  $N$  is the number of degrees of freedom,  $\lambda$  is the real eigenvalue corresponding to the saddle coordinates (*reactive coordinates* for chemical reactions) spanned by  $(q_1, p_1)$ , and  $\omega_k$  are the frequencies associated with the center coordinates (*bath coordinates* for chemical reactions) spanned by the pair  $(q_k, p_k)$  for  $k = 2, \dots, N$ .

Next, by fixing the energy level to  $h \in \mathbb{R}^+$  and constant  $c \in \mathbb{R}^+$ , we can define a codimension-1 region  $\mathcal{R} \subset \mathbb{R}^{2N}$  in the full phase space by the conditions

$$H_2(q_1, p_2, \dots, q_N, p_N) = h \quad \text{and} \quad |p_1 - q_1| \leq c. \quad (2)$$

This implies that  $\mathcal{R}$  is homeomorphic to the product of a  $(2N - 2)$  sphere and an interval  $I$ , that is,  $\mathcal{R} \cong \mathcal{S}^{2N-2} \times I$ , where the  $\mathcal{S}^{2N-2}$  is given by

$$\frac{\lambda}{4} (q_1 + p_1)^2 + \sum_{k=2}^N \frac{\omega_k}{2} (q_k^2 + p_k^2) = h + \frac{\lambda}{4} (p_1 - q_1)^2. \quad (3)$$

The sphere of  $\mathcal{R}$  at the middle of the equilibrium region, where  $p_1 - q_1 = 0$

$$\mathcal{M}_h^{2N-2} = \left\{ (q, p) \mid \lambda p_1^2 + \sum_{k=2}^N \frac{\omega_k}{2} (q_k^2 + p_k^2) = h \right\}, \quad (4)$$

corresponds to the transition state in chemical reactions (and other systems with similar Hamiltonian structure [7,10,11]).

The following phase space structures and their geometry are relevant for understanding transition across the saddle.

### A. NHIM

The point  $q_1 = p_1 = 0$  in the saddle projection corresponds to an invariant  $(2N - 3)$  sphere,  $\mathcal{M}_h^{2N-3}$ , of periodic

and quasiperiodic orbits in  $\mathcal{R}$ , and is given by

$$\sum_{k=2}^N \frac{\omega_k}{2} (q_k^2 + p_k^2) = h, \quad q_1 = p_1 = 0. \quad (5)$$

This is known as the *normally hyperbolic invariant manifold* (NHIM), which has the property that the manifold has a “saddlelike” stability in directions transverse to the manifold, and initial conditions on this surface evolve on it for  $t \rightarrow \pm\infty$ . The role of unstable periodic orbits in the four-dimensional phase space (or more generally the NHIM in the  $2N$ -dimensional phase space) in transition between potential wells is acting as an anchor for constructing the separatrices of transit and nontransit trajectories.

### B. Separatrix

The four half-open segments on the axes,  $q_1 p_1 = 0$ , correspond to four high-dimensional cylinders of orbits asymptotic to this invariant  $\mathcal{S}^{2N-3}$  either as time increases ( $p_1 = 0$ ) or as time decreases ( $q_1 = 0$ ). These are called *asymptotic* orbits and they form the stable and the unstable invariant manifolds of  $\mathcal{S}^{2N-3}$ . The stable manifolds,  $\mathcal{W}_\pm^s(\mathcal{S}^{2N-3})$ , are given by

$$\sum_{k=2}^N \frac{\omega_k}{2} (q_k^2 + p_k^2) = h, \quad q_1 = 0, \quad (6)$$

where  $\pm$  denotes the left and right branches of the stable manifold attached to the NHIM. Similarly, unstable manifolds are constructed and are shown in the saddle space in Fig. 1 as four orbits labeled  $M$ . These form the “spherical cylinders” of orbits asymptotic to the invariant  $(2N - 3)$  sphere. Topologically, both invariant manifolds have the structure of  $(2N - 2)$ -dimensional “tubes” ( $\mathcal{S}^{2N-3} \times \mathbb{R}$ ) inside the  $(2N - 1)$ -dimensional energy surface. Thus, they separate two distinct types of motion: transit and nontransit trajectories. While a transition trajectory, passing from one region to another, lies inside the  $(2N - 2)$ -dimensional manifold, the nontransition trajectories, bouncing back to their current region of motion, are those outside the manifold.

For a value of the energy just above that of the saddle, the nonlinear motion in the equilibrium region  $\mathcal{R}$  is qualitatively the same as the linearized picture above [5,29,30].

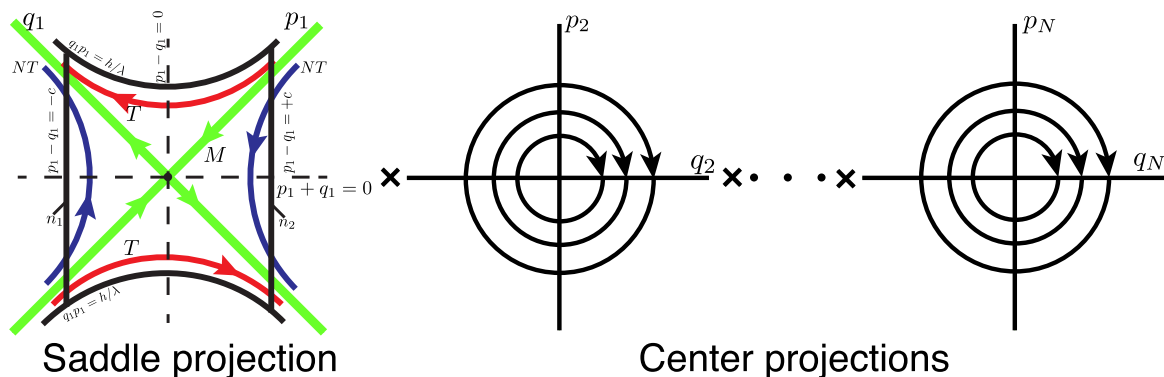


FIG. 1. The flow in the region  $\mathcal{R}$  can be separated into saddle  $\times$  center  $\times \dots \times$  center. On the left, the saddle projection is shown on the  $(q_1, p_1)$  plane. The NHIM (black dot at the origin), the asymptotic orbits on the stable and unstable manifolds ( $M$ ), two transition trajectories ( $T$ ), and two nontransition trajectories ( $NT$ ).

For example, the NHIM for the nonlinear system, which corresponds to the  $(2N - 3)$  sphere in (5) for the linearized system, is given by

$$\mathcal{M}_h^{2N-3} = \left\{ (q, p) \mid \sum_{k=2}^N \frac{\omega_k}{2} (q_k^2 + p_k^2) + f(q_2, p_2, \dots, q_n, p_n) = h, \quad q_1 = p_1 = 0 \right\}, \quad (7)$$

where  $f$  is at least of third order. Here,  $(q_2, p_2, \dots, q_n, p_n)$  are normal form coordinates and are related to the linearized coordinates via a near-identity transformation. In the neighborhood of the equilibrium point, since the higher-order terms in  $f$  are negligible compared to the second-order terms, the  $(2N - 3)$  sphere for the linear problem is a deformed sphere for the nonlinear problem. Moreover, since the NHIMs persist for higher energies, this deformed sphere  $\mathcal{M}_h^{2N-3}$  still has stable and unstable invariant manifolds that are given by

$$\mathcal{W}_\pm^s(\mathcal{M}_h^{2N-3}) = \left\{ (q, p) \mid \sum_{k=2}^N \frac{\omega_k}{2} (q_k^2 + p_k^2) + f(q_2, p_2, \dots, q_n, p_n) = h, \quad q_1 = 0 \right\},$$

$$\mathcal{W}_\pm^u(\mathcal{M}_h^{2N-3}) = \left\{ (q, p) \mid \sum_{k=2}^N \frac{\omega_k}{2} (q_k^2 + p_k^2) + f(q_2, p_2, \dots, q_n, p_n) = h, \quad p_1 = 0 \right\}. \quad (8)$$

This geometric insight is useful for developing numerical methods for *globalization* of the invariant manifolds using numerical continuation [31].

Now, we briefly describe the techniques that can be used to quantify and visualize the high-dimensional invariant manifolds. For positive value of excess energy, one can use a normal form computation to obtain higher-order terms of (7) and (8). A brief overview of this approach is given in [32] along with applications and results obtained using the computational tool for the Hamiltonian normal form. Another approach is to sample points on these manifolds since the geometry of the manifold is known near the equilibrium point. One would start by taking Poincaré sections and using normal form theory that involves high-order expansions around a saddle  $\times$  center  $\cdots \times$  center equilibrium. For example, in 3 DOF, the NHIM has topology  $\mathbb{S}^3$  and thus a tube cross section on a 4D Poincaré section will have topology  $\mathbb{S}^3$  for which it is possible to obtain an inside and outside. If  $x = \text{const}$  defines the Poincaré section, then one can project the  $\mathbb{S}^3$  structure to two transverse planes,  $(y, p_y)$  and  $(z, p_z)$ . On each plane, the projection appears as a disk, but because of the  $\mathbb{S}^3$  topology, any point in the  $(z, p_z)$  projection corresponds to a topological circle in the  $(y, p_y)$  (and vice versa), and from this one can determine which initial conditions are inside, and thus transit trajectories, as has been performed previously [28,33].

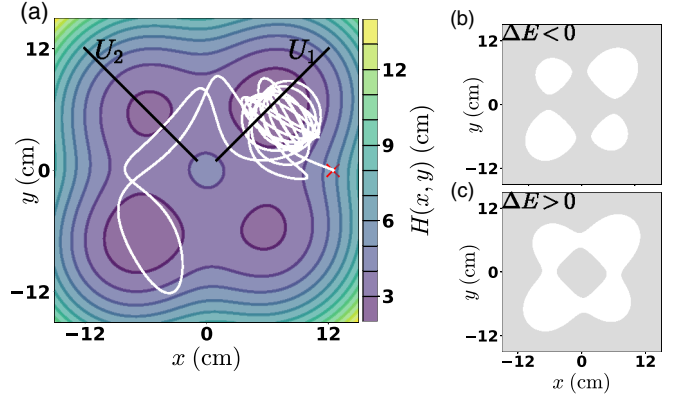


FIG. 2. (a) A typical experimental trajectory, shown in white, on the potential energy surface where the contours denote isoheights of the surface. This instance of the trajectory was traced by the ball released from rest, marked by a red cross. Parts (b) and (c) show the energetically accessible region projected on the configuration space in white for  $\Delta E < 0$ :  $\Delta E = -100 \text{ (cm/s)}^2$  and  $\Delta E > 0$ :  $\Delta E = 100 \text{ (cm/s)}^2$ , respectively.

### III. MODEL OF THE 2 DOF EXPERIMENTAL SYSTEM

The initial mathematical model of the transition behavior of a rolling ball on the surface,  $H(x, y)$ , shown in Fig. 5(b), is described in [34]. The equations of motion are obtained from the Hamiltonian,  $\mathcal{H}(x, y, p_x, p_y) = T(x, y, p_x, p_y) + V(x, y)$ , where mass factors out and where the kinetic energy (translational and rotational for a ball rolling without slipping) is

$$T = \frac{5}{14} \frac{(1 + H_y^2)p_x^2 + (1 + H_x^2)p_y^2 - 2H_xH_y p_x p_y}{1 + H_x^2 + H_y^2}, \quad (9)$$

where  $H_{(.)} = \frac{\partial H}{\partial (.)}$ . The potential energy is  $V(x, y) = gH(x, y)$ , where  $g = 981 \text{ cm/s}^2$  is the gravitational acceleration, and the height function is

$$H = \alpha(x^2 + y^2) - \beta(\sqrt{x^2 + \gamma} + \sqrt{y^2 + \gamma}) - \xi xy + H_0. \quad (10)$$

This is the analytical function for the machined surface shown in Fig. 5(b) and the isoheights shown in Fig. 2(a). We use parameter values  $(\alpha, \beta, \gamma, \xi, H_0) = (0.07, 1.017, 15.103, 0.00656, 12.065)$  in the appropriate units [31].

Let  $\mathcal{M}(E)$  be the *energy manifold* in the 4D phase space given by setting the total energy equal to a constant,  $E$ , i.e.,  $\mathcal{M}(E) = \{(x, y, p_x, p_y) \in \mathbb{R}^4 \mid \mathcal{H}(x, y, p_x, p_y) = E\}$ . The projection of the energy manifold onto the  $(x, y)$  configuration space is the region of energetically possible motion for a mass with energy  $E$ , and is given by  $M(E) = \{(x, y) \mid V(x, y) \leq E\}$ . The boundary of  $M(E)$  is the zero velocity curve and is defined as the locus of points in the  $(x, y)$  plane where the kinetic energy is zero. The mass is only able to move on the side of the curve where the kinetic energy is positive, shown as white regions in Figs. 2(b) and 2(c). The critical energy for transition,  $E_e$ , is the energy of the rank-1 saddle points in each bottleneck, which are all equal. This energy divides the global behavior of the mass into two cases,

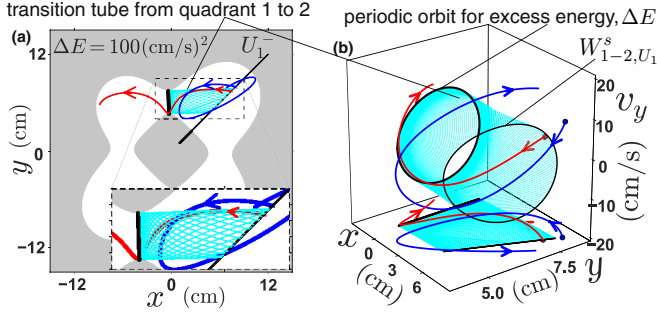


FIG. 3. (a) For a fixed excess energy,  $\Delta E$ , above the critical value  $E_e$ , the permissible regions (in white) are connected by a bottleneck around the saddle equilibria. All motion from the well in quadrant 1 to quadrant 2 must occur through the interior of a stable manifold associated with an unstable periodic orbit in the bottleneck between the quadrants, seen as a 2D configuration space projection of the 3D energy manifold. We show the stable manifold (cyan) and the periodic orbit (black) for an excess energy of  $\Delta E = 100 \text{ (cm/s)}^2$ . A trajectory crossing the  $U_1^-$  section inside the stable manifold will transition (red) into the quadrant 2 well, while one that is outside (blue) stays inside quadrant 1. The zoomed-in inset in the figure shows the structure of the manifold and how precisely the separatrix divides transition and nontransition trajectories. (b) In the  $(x, y, v_y)$  projection, the phase space conduit for imminent transition from quadrant 1 to 2 is the stable manifold (cyan) of geometry  $\mathbb{R}^1 \times \mathbb{S}^1$  (i.e., a cylinder). The same example trajectories (red and blue) as in (a) that exhibit transition and nontransition behavior starting inside and outside the stable manifold, respectively, are shown in the 3D projection and projected on the  $(x, y)$  configuration space. A movie of a nested sequence of these manifolds can be found at Ref. [35].

according to the sign of the excess energy above the saddle,  $\Delta E = E - E_e$ :

*Case 1.*  $\Delta E < 0$ —the mass is safe against transition and remains inside the starting well since potential wells are not energetically connected [Fig. 2(b)].

*Case 2.*  $\Delta E > 0$ —the mass can transition by crossing the bottlenecks that open up around the saddle points, permitting transition between the potential wells [Figs. 2(c) and Fig. 3(a) show this case].

Thus, transition between wells can occur when  $\Delta E > 0$ , and this constitutes a necessary condition. The sufficient condition for transition to occur is when a trajectory enters a codimension-1 invariant manifold associated with the unstable periodic orbit in the bottleneck as shown by nontransition and transition trajectories in Fig. 3(a) [18]. In 2 DOF systems, the periodic orbit residing in the bottleneck has an invariant manifold that is codimension-1 in the energy manifold and has topology  $\mathbb{R}^1 \times \mathbb{S}^1$ , which is a cylinder or tube [31]. This implies that the transverse intersection of these manifolds with Poincaré surfaces-of-sections,  $U_1$  and  $U_2$ , is topologically  $\mathbb{S}^1$ , a closed curve [7, 10, 18]. All the trajectories transitioning to a different potential well (or having just transitioned into the well) are inside a tube manifold, for example as shown in Fig. 3(b) [18, 19]. For every  $\Delta E > 0$ , the tubes in phase space [or more precisely, within  $\mathcal{M}(E)$ ] that lead to transition are the stable (and that lead to entry are the unstable) manifolds associated with the unstable periodic orbit of energy  $E$ . Thus, the mass's imminent transition

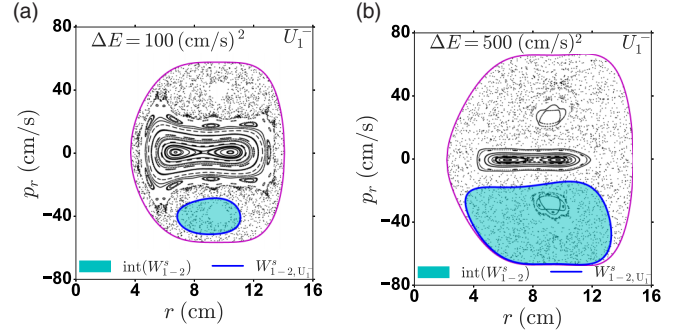


FIG. 4. Poincaré section,  $P^- : U_1^- \rightarrow U_1^+$ , of trajectories where  $U_1^- := \{(r, p_r) | \theta = \pi/4, p_\theta > 0\}$ , at excess energy (a)  $\Delta E = 100 \text{ (cm/s)}^2$  and (b)  $\Delta E = 500 \text{ (cm/s)}^2$ . The blue curves with a cyan interior denote the intersection of the tube manifold (stable) associated with the unstable periodic orbit with  $U_1^-$ . It should be noted that these manifolds act as a boundary between transition and nontransition trajectories, and may include KAM tori spanning more than one well. The interior of the manifolds,  $\text{int}(\cdot)$ , denotes the region of imminent transition to the quadrant 2 from quadrant 1. A movie showing the Poincaré section for a range of excess energy can be found at Ref. [36].

between adjacent wells can be predicted by considering where it crosses  $U_1$ , as shown in Fig. 4, relative to the intersection of the tube manifold. Furthermore, nested energy manifolds have corresponding nested stable and unstable manifolds that mediate transition. To simplify analysis, we focus only on the transition of trajectories that intersect  $U_1$  in the first quadrant. This surface-of-section is best described in polar coordinates  $(r, \theta, p_r, p_\theta)$ ;  $U_1^\pm = \{(r, p_r) | \theta = \frac{\pi}{4}, -\text{sgn}(p_\theta) = \pm 1\}$ , where  $+$  and  $-$  denote motion to the right and left of the section, respectively [31]. This Hamiltonian flow on  $U_1^\pm$  defines a symplectic map with typical features such as KAM tori and chaotic regions, shown in Fig. 4 for two values of excess energy.

Based on these phase space conduits that lead to transition, we would like to calculate what fraction of the energetically permissible trajectories will transition from or into a given well. This can be answered in part by calculating the transition rate of trajectories crossing the rank-1 saddle in the bottleneck connecting the wells. For computing this rate—surface integral of trajectories crossing a bounded surface per unit time—we use the geometry of the tube manifold cross section on the Poincaré section. For low excess energy, this computation is based on the theory of flux over a rank-1 saddle [37], which corresponds to the action integral around the periodic orbit at energy  $\Delta E$ . By the Poincaré integral invariant [38], this action is preserved for symplectic maps, such as  $P^\pm : U_1^\pm \rightarrow U_1^\pm$ , and is equivalent to computing the area of the tube manifold's intersection with the surface-of-section. The transition fraction at each energy,  $p_{\text{trans}}(\Delta E)$ , is calculated by the fraction of energetically permissible trajectories at a given excess energy,  $\Delta E$ , that will transition. This is given by the ratio of the cross sections on  $U_1$  of the tube to the energy surface. The transition area, to leading order in  $\Delta E$  [37], is given by  $A_{\text{trans}} = T_{\text{po}} \Delta E$ , where  $T_{\text{po}} = 2\pi/\omega$  is the period of the periodic orbits of small energy in the bottleneck, where  $\omega$  is the imaginary part of the complex-conjugate pair of eigenvalues resulting from the

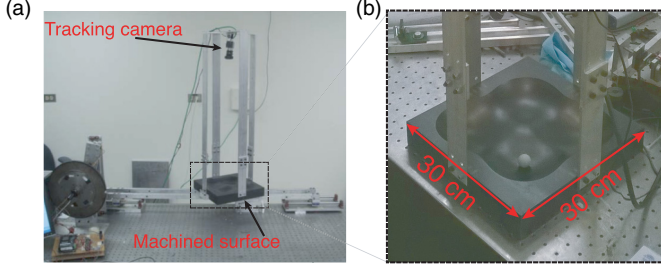


FIG. 5. (a), (b) Experimental apparatus showing the machined surface, tracking camera, and the rubber coated steel ball.

linearization about the saddle equilibrium point [37]. The area of the energy surface projection on  $U_1$ , to leading order in  $\Delta E > 0$ , is  $A_E = A_0 + \tau \Delta E$ , where

$$A_0 = 2 \int_{r_{\min}}^{r_{\max}} \sqrt{\frac{14}{5} [E_e - gH(r)] [1 + 4H_r^2(r)]} dr \quad (11)$$

$$\text{and } \tau = \int_{r_{\min}}^{r_{\max}} \sqrt{\frac{14}{5} \frac{[1 + 4H_r^2(r)]}{[E_e - gH(r)]}} dr. \quad (12)$$

The transition fraction, under the well-mixed assumption mentioned earlier, is given in 2 DOF by

$$p_{\text{trans}} = \frac{A_{\text{trans}}}{A_E} = \frac{T_{\text{po}}}{A_0} \Delta E \left( 1 - \frac{\tau}{A_0} \Delta E + O(\Delta E^2) \right). \quad (13)$$

For small positive excess energy, the predicted growth rate is  $T_{\text{po}}/A_0 \approx 0.87 \times 10^{-3} \text{ (s/cm)}^2$ . For larger values of  $\Delta E$ , the cross-sectional areas are computed numerically using Green's theorem; see Fig. 6(b).

As with any physical experiment, there is dissipation present, but over the timescale of interest, the motion approximately conserves energy. We compare  $\delta E$ , the typical energy lost during a transition, with the typical excess energy,  $\Delta E > 0$ , when transitions are possible. The timescale of interest,  $t_{\text{trans}}$ , corresponds to the time between crossing  $U_1$  and transitioning across the saddle into a neighboring well. The energy loss over  $t_{\text{trans}}$  in terms of the measured damping ratio  $\zeta \approx 0.025$  is  $\delta E \approx \pi \zeta v^2(\Delta E)$ , where the squared-velocity  $v^2(\Delta E)$  is approximated through the total energy. For our experimental trajectories, all starting at  $\Delta E > 1000 \text{ (cm/s)}^2$ , we find  $\delta E/\Delta E \ll 1$ , suggesting the appropriateness of the assumption of short-time conservative dynamics to study transition between wells [7,10].

#### IV. EXPERIMENTAL SETUP

We designed a surface that has four wells, one in each quadrant, with saddles connecting the neighboring quadrants [shown in Fig. 5(b)]. The surface has four stable and five saddle (four rank-1 and one rank-2) equilibrium points. Interwell first-order transitions are defined as crossing the rank-1 saddles between the wells. On this high-precision machined surface, accurate to within 0.003 mm and made using stock polycarbonate, a small rubber-coated spherical steel mass released from rest can roll without slipping under the influence of gravity. The mass is released from different locations on the machined surface to generate experimental trajectories.

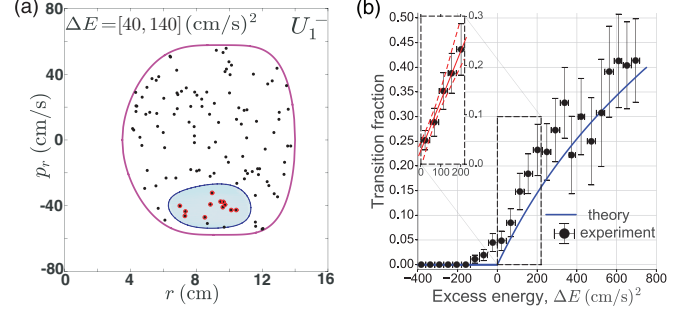


FIG. 6. (a) On the Poincaré section,  $U_1^-$ , we show a narrow range of energy  $[\Delta E \in (40, 140) \text{ (cm/s)}^2]$  and label intersecting trajectories as no transition (black) and imminent transition (red) to quadrant 2, based on their measured behavior. The stable invariant manifold associated with the bottleneck periodic orbit at excess energy,  $\Delta E = 140 \text{ (cm/s)}^2$ , intersects the Poincaré section,  $U_1^-$ , along the blue curve. Its interior is shown in cyan and includes the experimental transition trajectories. The outer closed curve (magenta) is the intersection of the boundary of the energy surface  $\mathcal{M}(\Delta E)$  with  $U_1^-$ . (b) Transition fraction of trajectories as a function of excess energy above the saddle. The theoretical result is shown (blue curve) and experimental values are shown as filled circles (black) with error bars. For small excess energy above critical ( $\Delta E = 0$ ), the transition fraction shows linear growth (see inset) with slope  $1.0 \pm 0.23 \times 10^{-3} \text{ (s/cm)}^2$  and shows agreement with the analytical result (13). A movie of increasing transition area on the Poincaré section,  $U_1^-$ , can be found at Ref. [39].

The mass is tracked using a Prosilica GC640 digital camera mounted on a rigid frame attached to the surface as shown in Fig. 5(a), with a pixel resolution of about 0.16 cm. The tracking is done by capturing black and white images at 50 Hz, and calculating the coordinates of the mass's geometrical center. We recorded 120 experimental trajectories of about 10 s long, only using data after waiting at least the Lyapunov time of  $\approx 0.4 \text{ s}$  [34] ensuring that the trajectories were well-mixed in the phase space. To analyze the fraction of trajectories that leave or enter a well, we obtain approximately 4000 intersections with a Poincaré surface-of-section,  $U_1$ , shown as a black line, for the analyzed range of energy. One such trajectory is shown in white in Fig. 2(a). These intersections are then sorted according to energy. The intersection points on  $U_1$  are classified as a transition from quadrant 1 to 2 if the trajectory, followed forward in time, leaves quadrant 1. A total of 400 transition events were recorded.

#### V. RESULTS

For each of the recorded trajectories, we detect intersections with  $U_1$  and determine the instantaneous  $\Delta E$ . Grouping intersection points by energy [e.g., Fig. 6(a)], we get an experimental transition fraction, Fig. 6(b), by dividing points that transitioned by the total in each energy range. Despite the experimental uncertainty from the image analysis, agreement between observed and predicted values is satisfactory. In fact, a linear fit of the experimental results for small excess energy gives a slope close to that predicted by (13) within the margin of error. Furthermore, the clustering of observed transitioning trajectories in each energy range, as in Fig. 6(a), is consistent

with the theory of tube dynamics. The predicted transition regions in each energy range account for more than 99% of the observed transition trajectories.

## VI. CONCLUSIONS

We considered a macroscopic 2 DOF experimental system showing transitions between potential wells and a dynamical systems theory of the conduits that mediate those transitions [7,10,18]. The experimental validation presented here confirms the robustness of the conduits between multi-stable regions, even in the presence of nonconservative forces, providing a strong footing for predicting transitions in a

wide range of physical systems. Given the fragility of other structures to dissipation (for example, KAM tori and periodic orbits), these phase space conduits of transition may be among the most robust features to be found in experiments of autonomous multiple DOF systems. Furthermore, this study lays the groundwork for experimental validation for an  $N = 3$  or more DOF system, such as ship dynamics [8–10,40], buckling of beams [7] and geodesic lattice domes, hanging roller pins, isomerization, and roaming reactions [41,42].

## ACKNOWLEDGMENTS

S.D.R. and L.N.V. thank the NSF for partially funding this work through Grants No. 1537349 and No. 1537425.

- 
- [1] C. Jaffé, D. Farrelly, and T. Uzer, *Phys. Rev. Lett.* **84**, 610 (2000).
- [2] B. Eckhardt, *J. Phys. A* **28**, 3469 (1995).
- [3] T. Komatsuzaki and R. S. Berry, *Proc. Natl. Acad. Sci. (U.S.A.)* **98**, 7666 (2001).
- [4] T. Komatsuzaki and R. S. Berry, *J. Chem. Phys.* **110**, 9160 (1999).
- [5] S. Wiggins, L. Wiesenfeld, C. Jaffé, and T. Uzer, *Phys. Rev. Lett.* **86**, 5478 (2001).
- [6] P. Collins, G. S. Ezra, and S. Wiggins, *Phys. Rev. E* **86**, 056218 (2012).
- [7] J. Zhong, L. N. Virgin, and S. D. Ross, *Int. J. Mech. Sci.* **149**, 413 (2018).
- [8] L. N. Virgin, *Dyn. Stab. Syst.* **4**, 56 (1989).
- [9] J. M. T. Thompson and J. R. de Souza, *Proc. R. Soc. Lond. A* **452**, 2527 (1996).
- [10] S. Naik and S. D. Ross, *Commun. Nonlin. Sci.* **47**, 48 (2017).
- [11] C. Jaffé, S. D. Ross, M. W. Lo, J. E. Marsden, D. Farrelly, and T. Uzer, *Phys. Rev. Lett.* **89**, 011101 (2002).
- [12] M. Dellnitz, O. Junge, M. W. Lo, J. E. Marsden, K. Padberg, R. Preis, S. D. Ross, and B. Thiere, *Phys. Rev. Lett.* **94**, 231102 (2005).
- [13] S. D. Ross, in *Libration Point Orbits and Applications*, edited by G. Gómez, M. W. Lo, and J. J. Masdemont (World Scientific, Singapore, 2003), pp. 637–652.
- [14] H. P. de Oliveira, A. M. Ozorio de Almeida, I. Damião Soares, and E. V. Tonini, *Phys. Rev. D* **65**, 083511 (2002).
- [15] L. N. Virgin and L. A. Cartee, *Int. J. Nonlin. Mech.* **26**, 449 (1991).
- [16] J. A. Gottwald, L. N. Virgin, and E. H. Dowell, *J. Sound Vib.* **187**, 133 (1995).
- [17] J. Novick, M. L. Keeler, J. Giefer, and J. B. Delos, *Phys. Rev. E* **85**, 016205 (2012).
- [18] W. S. Koon, M. W. Lo, J. E. Marsden, and S. D. Ross, *Chaos* **10**, 427 (2000).
- [19] F. Gabern, W. S. Koon, J. E. Marsden, S. D. Ross, and T. Yanao, *Few-Body Syst.* **38**, 167 (2006).
- [20] A. M. Ozorio de Almeida, N. De Leon, M. A. Mehta, and C. C. Marston, *Physica D* **46**, 265 (1990).
- [21] N. De Leon, M. A. Mehta, and R. Q. Topper, *J. Chem. Phys.* **94**, 8310 (1991).
- [22] C. C. Marston and N. De Leon, *J. Chem. Phys.* **91**, 3392 (1989).
- [23] O. Baskan, M. F. M. Speetjens, G. Metcalfe, and H. J. H. Clercx, *Chaos* **25**, 103106 (2015).
- [24] O. Baskan, M. F. M. Speetjens, G. Metcalfe, and H. J. H. Clercx, *Eur. J. Mech. B/Fluids* **57**, 1 (2016).
- [25] A. Figueroa, S. Cuevas, and E. Ramos, *J. Fluid Mech.* **815**, 415 (2017).
- [26] E. S. Gawlik, J. E. Marsden, P. C. Du Toit, and S. Campagnola, *Celest. Mech. Dynam. Astron.* **103**, 227 (2009).
- [27] K. Onozaki, H. Yoshimura, and S. D. Ross, *Adv. Space Res.* **60**, 2117 (2017).
- [28] F. Gabern, W. S. Koon, J. E. Marsden, and S. D. Ross, *Physica D* **211**, 391 (2005).
- [29] J. Moser, *Commun. Pure Appl. Math.* **11**, 257 (1958).
- [30] H. Waalkens and S. Wiggins, *Reg. Chaotic Dyn.* **15**, 1 (2010).
- [31] See Supplemental Material at <http://link.aps.org/supplemental/10.1103/PhysRevE.98.052214> for derivation of the equations of motion and the computational approach used to obtain the invariant manifolds.
- [32] S. Wiggins, in *IUTAM Symposium on Hamiltonian Dynamics, Vortex Structures, Turbulence*, edited by A. V. Borisov, V. V. Kozlov, I. S. Mamaev, and M. A. Sokolovskiy (Springer, Dordrecht, 2008), pp. 189–203. A. D. Burbanks, S. Wiggins, H. Waalkens, and R. Schubert, Background and documentation of software for computing hamiltonian normal forms (2008), software for normal form is available at <https://github.com/PeterCollins/NormalForm>.
- [33] G. Gómez, W. S. Koon, M. W. Lo, J. E. Marsden, J. Masdemont, and S. D. Ross, *Nonlinearity* **17**, 1571 (2004).
- [34] L. N. Virgin, T. C. Lyman, and R. B. Davis, *Am. J. Phys.* **78**, 250 (2010).
- [35] <https://youtu.be/gMqrFX2JkLU>.
- [36] <https://youtu.be/sNvgXCrX6oo>.
- [37] R. S. MacKay, *Phys. Lett. A* **145**, 425 (1990).
- [38] J. D. Meiss, *Rev. Mod. Phys.* **64**, 795 (1992).
- [39] <https://youtu.be/YZKYx0N9Zug>.
- [40] L. McCue and A. Troesch, *Ocean Engineering* **32**, 1608 (2005); **33**, 1796 (2006).
- [41] F. A. L. Mauguère, P. Collins, G. S. Ezra, S. C. Farantos, and S. Wiggins, *Theor. Chem. Acc.* **133** (2014).
- [42] J. M. Bowman and P. L. Houston, *Chem. Soc. Rev.* **46**, 7615 (2017).